geosciences

MDPI

Article

Experimental and Numerical Investigation of a Dissipative Connection for the Seismic Retrofit of Precast RC Industrial Sheds

Virginio Quaglini [1,*], Carlo Pettorruso [1], Eleonora Bruschi [1] and Luca Mari [2]

[1] Politecnico di Milano, Department of Architecture, Built Environment and Construction Engineering ABC, 20133 Milan, Italy; carlo.pettorruso@polimi.it (C.P.); eleonora.bruschi@polimi.it (E.B.)
[2] DVS srl, 25121 Brescia, Italy; l.mari@dvs.vision
* Correspondence: virginio.quaglini@polimi.it; Tel.: +39-02-23994248

Abstract: Past earthquakes have highlighted the seismic vulnerability of prefabricated industrial sheds typical of past Italian building practices. Such buildings typically exhibited rigid collapse mechanisms due to the absence of rigid links between columns, beams, and roof elements. This study aims at presenting the experimental and numerical assessment of a novel dissipative connection system (DCS) designed to improve the seismic performance of prefabricated sheds. The device, which is placed on the top of columns, exploits the movement of a rigid slider on a sloped surface to dissipate seismic energy and control the lateral displacement of the beam, and to provide a recentering effect at the end of the earthquake. The backbone curve of the DCS, and the effect of vertical load, sliding velocity, and number of cycles were assessed in experimental tests conducted on a scaled prototype, according to a test protocol designed accounting for similarity requirements. In the second part of the study, non-linear dynamic analyses were performed on a finite element model of a portal frame implementing, at beam-column joints, either the DCS or a pure friction connection. The results highlighted the effectiveness of the DCS in controlling beam-to-column displacements, reducing shear forces on the top of columns, and limiting residual displacements that can accrue during ground motion sequences.

Keywords: prefabricated sheds; energy dissipation; seismic retrofit; beam-to-column connection; recentering; reinforced concrete

Citation: Quaglini, V.; Pettorruso, C.; Bruschi, E.; Mari, L. Experimental and Numerical Investigation of a Dissipative Connection for the Seismic Retrofit of Precast RC Industrial Sheds. *Geosciences* **2022**, *12*, 25. https://doi.org/10.3390/geosciences12010025

Academic Editors: Antonio Formisano, Luigi Sorrentino, Maria Zucconi and Jesus Martinez-Frias

Received: 30 November 2021
Accepted: 4 January 2022
Published: 6 January 2022

1. Introduction

Recent earthquakes in Italy have dramatically reaffirmed the seismic vulnerability of precast industrial buildings, typical of past Italian building practices, highlighting structural deficiencies primarily related to the mechanisms of transmission of horizontal loads between structural elements [1]. In Italy, the majority of industrial one-story and multistory facilities consist of precast reinforced concrete (RC) structures, as the use of precast concrete systems offers several advantages such as fast erection, reduced investment costs owing to prefabrication, high allowance for quality controls, and enhanced safety. However, the static scheme commonly adopted in the past represents the major drawback of this structural typology. In fact, joints between structural elements such as beams, columns, and roof elements were commonly realized in simple support or through pin-end connections with insufficient resistance to seismic loads [1].

The most paradigmatic event is perhaps the Emilia earthquake (2012), which hit an area in north Italy densely populated by productive activities, striking mainly industrial buildings constructed of precast reinforced concrete [2,3], and causing an overall economic damage of EUR 13.27 billion, with an estimated loss of income between EUR 3 and 3.8 billion [4]. The structural layout of the damaged buildings typically presented cantilevered monolithic precast columns, placed into discrete socket foundations on site, and grouted

with low strength grout. Pin-ended prestressed L-beams, inverted T-beams, or double pitched beams rested on column corbels or directly at the tops of the columns. According to the building code enforced at the time of construction, the strength of beam-to-column connections was based solely on friction force, without additional mechanical devices; neoprene pads were adopted at the beam-column joints only for long spans [5–7]. No secondary beams were placed orthogonally to the primary frames to ensure the three-dimensional responses of the buildings, which substantially behaved as a series of essentially two-dimensional portal frames. The most common failures, causing the collapse of entire portions of buildings, included drop of roof elements and precast beams due to the loss of support, and collapse of the forks at the top of columns caused by off-axis loads. Such damage patterns were mainly related to poor strength and ductility of connections or to lack of mechanical links preventing excessive deformations [1,2,8–11].

The usual design practice, at the time of construction of the damaged buildings, was essentially based on vertical static loads in combination with wind-induced and crane-induced horizontal loads. A horizontal load equal to 2% of the vertical load was accounted for in the design only starting from 1987 [5,6,12]. However, for some noncompulsory provisions released between the mid-60s and mid-70s, the first specific seismic provisions appeared in Italy in the early 1990s, and internationally recognized modern seismic concepts, such as capacity design, were endorsed only in 2008 [13]. Therefore, although the prefabrication of RC elements in Italy was an established technology, several industrial facilities left to shear friction the horizontal load transfer mechanism of beam-to-column and beam-to-floor connections, as they were designed without modern seismic concepts and prescriptions.

Moreover, in the current precast design practice for one-story or low-rise industrial buildings of no primary importance, the contractors prefer to use dry connections as seismic load transfer mechanisms between precast elements to reduce the on-site construction time and cost. In the overall Italian context, the most advanced typology of shear-resisting dry beam-to-column joints is represented by pinned dowel connections with concrete corbels and 5–10 mm thick neoprene pads. As a result of this hinged frame structural layout, the seismic demand is currently accommodated by cantilevered columns with large cross sections (up to 1000 × 1000 mm in the case of three-story buildings). In order to improve the seismic performance of poorly designed or deficient precast structures, a retrofit intervention needs to be planned and implemented at either local or global level. Local interventions usually consist of structural strengthening, applying rigid and resistant reinforcement that increase the capacity of weak elements; such a reinforcement can be made of either steel, or high-strength fibers embedded into a cementitious or a polymeric matrix [14]. Global interventions are implemented by inserting in the structure particular devices, which either reduce the seismic input by separating the motion of the superstructure from the motion of the ground (namely seismic isolation systems), or increase the total energy dissipation capacity (namely energy dissipation devices) [15,16] by concentrating on special elements out of the vertical load bearing frame the dissipation of most of the energy transmitted by the earthquake [17,18]. Examples of application of energy dissipation systems to the retrofit of industrial frames can be found in references [16,19–22].

Another issue is represented by the lack of provisions to recenter the structure at the end of an earthquake, avoiding offsets [19,23]. There is indeed significant field evidence of seismic sequences characterized by frequent medium-strong intensity ground motions following a strong mainshock after short intervals of time [24–30]. Even though the maximum displacement of the beam can be accommodated by the connection, residual displacements may build up during sequences of ground motions occurring in short times, limiting the capability of the structure to withstand aftershocks and future earthquakes.

Within the framework of global retrofit interventions, the study aims at introducing a novel dissipative connection system (DCS), designed to improve the behavior of beam-to-column connections and reduce the seismic vulnerability of precast RC industrial buildings [31]. The DCS, which is placed on the top of columns, exploits the movement

of a rigid block sliding on a sloped surface to provide horizontal stiffness and a certain recentering effect, and dissipates part of seismic energy by friction. The connection system has been investigated both experimentally and through numerical analyses, and the results of the assessment are presented and discussed.

2. Principle of the Dissipative Connection System

The dissipative connection system (DCS) is basically composed of two mating truncated-pyramidal steel plates, one concave and the other one convex in shape (Figure 1). Steel fixtures are also provided to firmly link the plates to prefabricated RC structural elements. The system is designed to be inserted at the column-beam joints of a precast building, and is intended to transmit vertical and horizontal loads at the node.

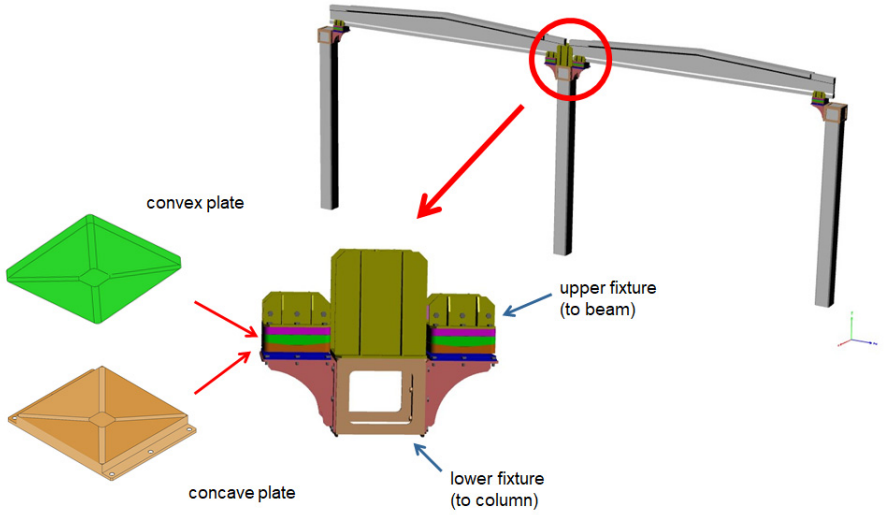

Figure 1. Sketch of the dissipative connection system and typical installation at beam-to-column joint.

The operation of the DCS is explained by referring to the motion of a rigid block on a sloped surface (Figure 2). An external force F must be provided to sustain the motion and overcome two resisting forces, namely: (1) the component (R_p) of the vertical force N acting parallel to the sloped surface; and (2) the friction shear force (R_μ) activated between the sliding block and the surface. The first contribution is always directed towards the lowest point of the sloped surface, while the direction of the friction force is opposed to the direction of sliding.

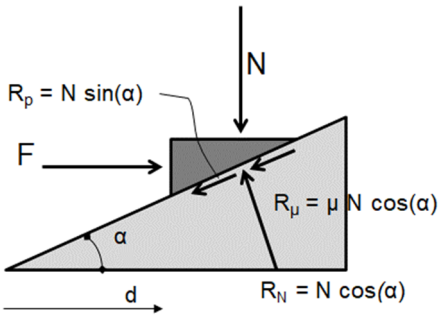

Figure 2. Mechanical model of a rigid block on sloped surface.

The horizontal movement of the beam, with respect to the column head caused from a horizontal action F, e.g., a seismic action, triggers the sliding of the convex plate on the

concave surface of the second element; owing to the truncated pyramidal shape of the two elements the theoretical force—displacement relationship takes the expression:

$$F = N\,[\sin\ \alpha \cdot \mathrm{sign}(d) + \mu\ \cos\ \alpha \cdot \mathrm{sign}(V)], \quad (1)$$

where F is the horizontal force, d is the horizontal deflection of the convex element with respect to the concave plate, N is the vertical load acting on the connection, α is the slope angle of the mating surfaces, μ is the coefficient of friction, V is the sliding velocity, and sign(·) is the sign function that extracts the sign of its argument (in the framework of Equation (1), sign(d) returns sign "+" when the displacement is positive, and sign "-" otherwise; sign(V) returns sign "+" when the velocity function is positive, i.e., the movement is directed away from the origin, and sign "-" when the velocity function is negative, i.e., the movement is directed towards the origin). For a cyclic motion of the convex plate with amplitude d_{bd}, a flag-shaped force—deflection curve as the ones illustrated in Figure 3 results. The force F holds constant during the motion of the plate in one direction, and changes its sign at motion reversal. By considering the half cycle for $0 \leq d \leq d_{bd}$ (), the coordinates of the corner points are: A (0; (sin α + μ cos α)·N); B (d_{bd}; (sin α + μ cos α)·N); C (d_{bd}; (sin α − μ cos α)·N); and D(0; (sin α − μ cos α)·N), respectively. For $-d_{bd} \leq d \leq 0$ the force changes its sign, and the curve is symmetric with respect to the origin of the axes. The area enclosed in the hysteresis loop counts 4 μ N d_{bd} and represents the energy dissipated by friction during the cycle.

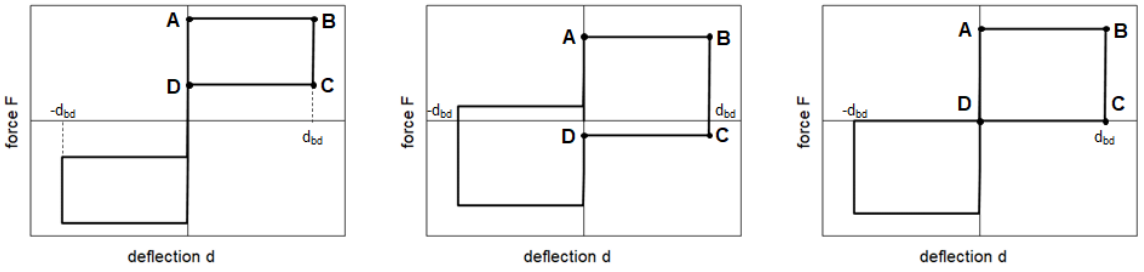

Figure 3. Backbone curves of the dissipative connection systems: (**a**) μ < tan(α); (**b**) μ > tan(α); (**c**) μ = tan(α).

Depending on the slope angle α and the friction coefficient μ, one of the possible three backbone curves shown in Figure 3 results:

- If μ < tan(α), the curve has the shape shown in Figure 3a: when sign(d) and sign(V) have different signs, sin(α) > μ cos(α) and the recentering force due to gravity prevails on the friction term. The device has a fair recentering behavior and naturally tends to return to the origin at the end of the seismic shake. Moreover, for a given angle α, this design choice limits the shear force on the top of the columns, but reduces the amount of dissipated energy, which is proportional to μ, and therefore increases the displacement;
- If μ > tan(α), the curve has the shape shown in Figure 3b: the friction shear force prevails over the restoring force due to the slope, which hampers the recentering capability of the connection. For a given angle α, this choice increases the shear force on the top of the columns, but reduces the maximum displacement by increasing the dissipation;
- If μ = tan(α), the curve has the shape shown in Figure 3c, corresponding to an elastic-perfectly plastic behavior. When sign(d) and sign(V) have different signs, sin(α) = μ cos(α) and the device has no inherent recentering capacity; however, it does not develop any resistance to an external recentering action, which can be due to, e.g., small vibrations occurring during the coda stage of the ground motion. For a

given angle α, this solution is likely to represent the best trade-off to control both maximum forces and displacements, and is implemented in the design of the DCS.

3. Materials and Methods

The mechanical behavior of the DCS was investigated both experimentally and numerically, in order to assess the actual force-deflection behavior and evaluate its performance under seismic loading.

The study is conducted by referring to a DCS rated for a vertical load N_d = 360 kN and a horizontal deflection d_{bd} = 60 mm. The angle of the sloped surfaces is $\alpha = 6°$ and the design friction coefficient is $\mu = 0.105$. With this choice, $\mu = \tan(6°)$, thereby resulting in a theoretical force—deflection curve as the one depicted in Figure 3c.

3.1. Experimental Investigation

In order to match the capacity of the testing equipment, the experimental characterization was performed on a prototype of the DCS scaled by a geometric factor $S_L = 0.4$ and fabricated in steel (i.e., the scale factor for modulus of elasticity is $S_E = 1$). By evoking the principle of similarity [32], scaling factors for all mechanical quantities were determined (Table 1). The main dimensions of the prototype are shown in Figure 4. Based on the assigned scaling factors, the design vertical load and the deflection of the scaled prototype resulted in $N_{d,s}$ = 57.6 kN and $d_{bd,s}$ = 24 mm, respectively. It must be noted that by applying similarity concepts, the nominal pressure acting on the contact surfaces between the mating plates (which can affect the coefficient of friction) is independent of the scale of the device.

Table 1. Scale factors assumed for the tests.

Quantity	Dimension	Scale Factor
Length	[L]	$S_L = 0.4$
Elastic Modulus	[F] [L]$^{-2}$	$S_E = 1.0$
Force	[F]	$S_F = (S_L)^2 = 0.16$
Pressure	[F] [L]$^{-2}$	$S_p = 1.0$
Displacement	[L]	$S_d = 0.4$
Time	[T]	$S_T = (S_L)^{1/2} = 0.6324$
Velocity	[L] [T]$^{-1}$	$S_V = (S_L)^{1/2} = 0.6324$
Frequency	[T]$^{-1}$	$S_f = (S_L)^{-1/2} = 1.5811$

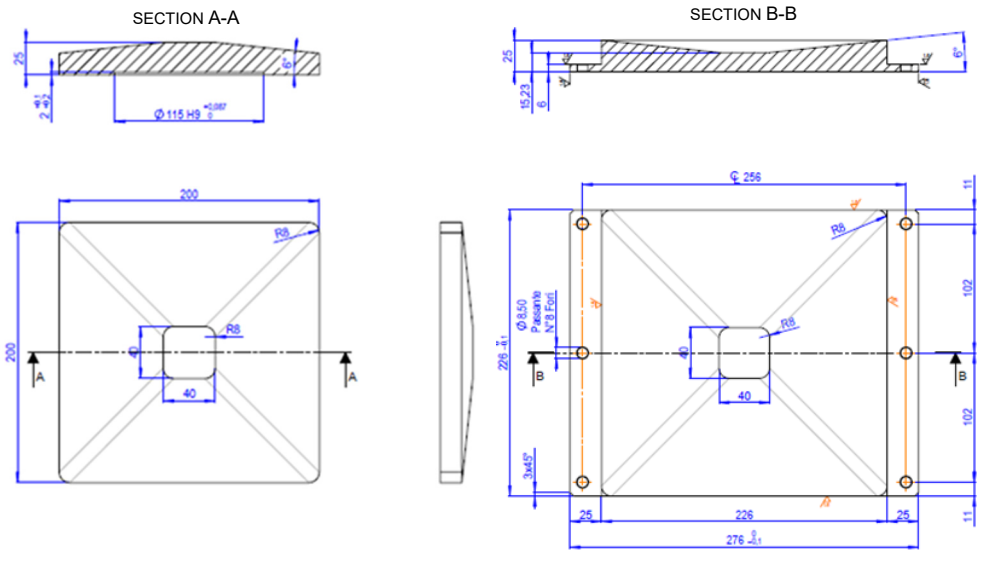

(**a**) (**b**)

Figure 4. Small scale prototype of the DCS: (**a**) convex plate; (**b**) concave plate. Units in mm.

The tests were conducted at the Materials Testing Laboratory of Politecnico di Milano, using a proprietary biaxial testing system designed for testing of scaled specimens of seismic isolators (Figure 5a). The system comprises a rigid frame with four columns and two fixed crossbeams, which form a closed ring wherein the forces are confined, and is provided with two servo-hydraulic actuators arranged orthogonally to each other, in order to apply a vertical load on the specimen and a concurrent horizontal deflection. The load capacity of the system is 500 kN in vertical direction and 75 kN in horizontal direction, and the horizontal displacement capacity is 100 mm (50 mm in either direction).

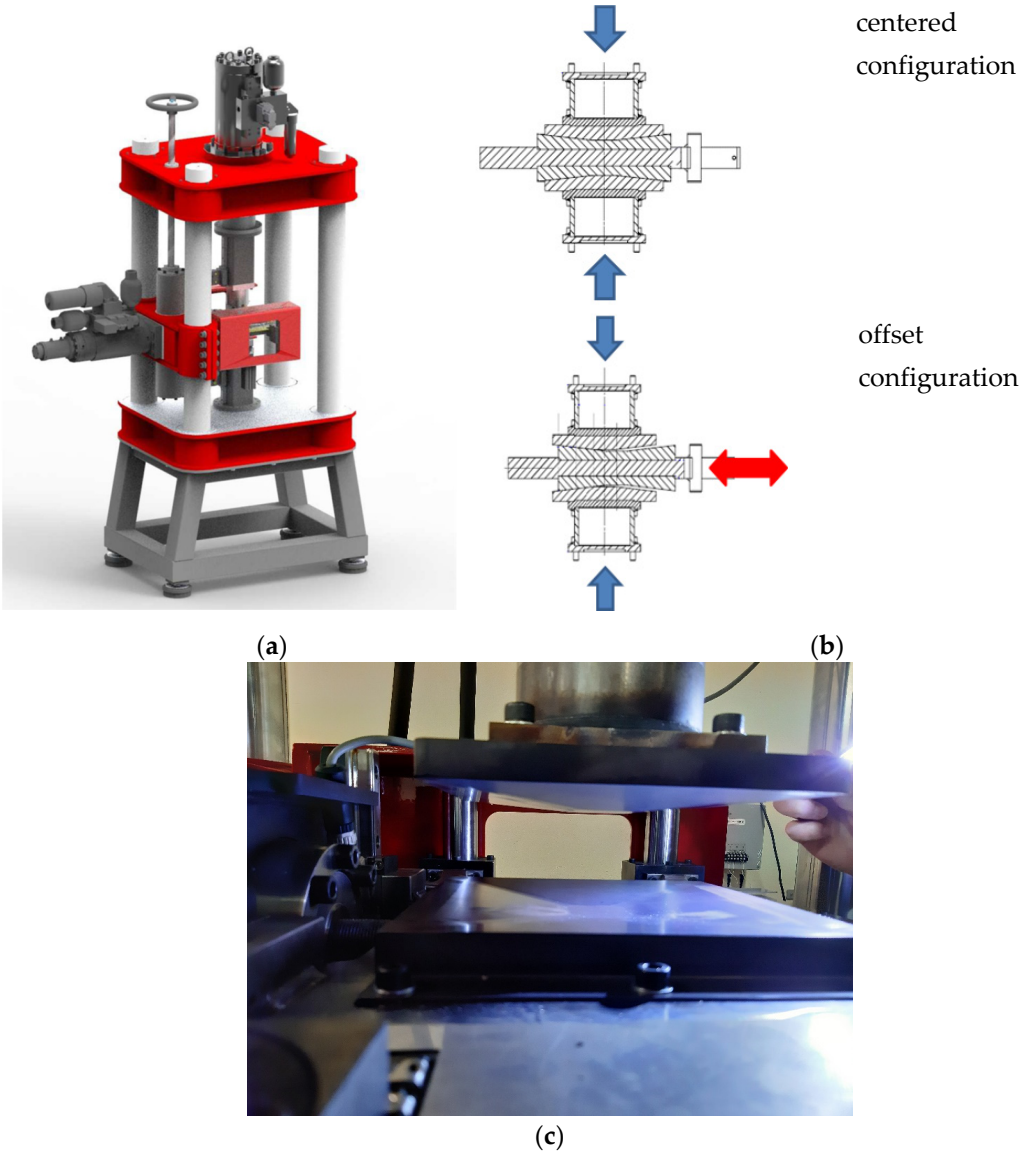

Figure 5. Experimental apparatus: (**a**) biaxial testing machine; (**b**) specimen setup; (**c**) picture of the specimen installed on the testing machine, with close-up of convex and concave plates.

In order to minimize the moment on the testing machine caused from the eccentricity of the vertical load applied on the prototype when the convex plate is in an offset configuration away from the center of the concave plate, the tests were performed on a set of two identical specimens, arranged in an upside-down configuration (Figure 5b): the concave elements of the two specimens were mounted on a plate moved by the horizontal actuator, while the two convex elements were clamped to the vertical actuator and the lower crossbeam, respectively. A close-up of the sloped surfaces of the concave and convex plates is shown in Figure 5c.

The mating surfaces of the prototypes were lubricated with a multipurpose grease containing molybdenum disulfide (MoS2), which was checked in preliminary tests to be able to provide the target coefficient of friction of 0.10. The tests were conducted by applying to the pair of specimens a vertical load N_S, which was kept constant during the test, and simultaneously imposing a horizontal deflection, performing cycles of amplitude d_S at a constant speed V_S. In total, three groups of tests were performed: (a) static tests (S), conducted at low velocity to investigate the influence of the vertical load, which was varied between 0.25 $N_{d,s}$ and 2.5 $N_{d,s}$; (b) dynamic tests (D), conducted at increasing speeds, to investigate the effect of velocity; and (c) static tests with rotation (R), where the movement of the convex plate was imposed along a direction rotated by $\theta = 45°$ with respect to the main axis of the prototype, i.e., along one of the four sloped edges of the truncated pyramidal geometry. The layout of the tests is reported in Table 2, while the reference system used to define the direction of loading is shown in Figure 6.

Table 2. Test layout.

ID	N_S [kN]	d_S [mm]	V_S [mm/s]	θ [°]	n [#]
Static Test (S)					
S1	14.4	24	0.672	0	3
S2	28.8	24	0.672	0	3
S3	57.6	24	0.672	0	3
S4	72.0	24	0.672	0	3
S5	86.4	24	0.672	0	3
S6	100.8	24	0.672	0	3
S7	115.2	24	0.672	0	3
S8	129.6	24	0.672	0	3
S9	144.0	24	0.672	0	3
Dynamic Test (D)					
D1a	28.8	24	3.36	0	5
D1b	28.8	24	6.72	0	5
D1c	28.8	24	16.8	0	5
D1d	28.8	24	33.6	0	5
D2a	57.6	24	3.36	0	20
Static Test with Rotation (R)					
R1	14.4	24	0.672	45	3
R2	28.8	24	0.672	45	3
R3	57.6	24	0.672	45	3

Parameters N_S, d_S, V_S, θ are defined in the main text; n is the number [#] of cycles.

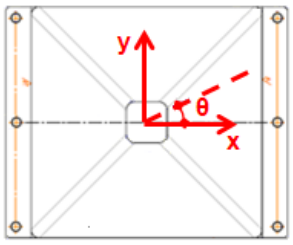

Figure 6. Reference system of the DCS.

3.2. Numerical Investigation

To assess the performance of the DCS and evaluate its effectiveness in comparison to the beam-to-column pure friction joint typical of past building practices, non-linear dynamic analyses of a prefabricated shed structure were performed.

The model consists of a two-dimensional portal frame comprising two 50 × 60 cm columns and a 50 × 80 cm beam, with geometry and overall dimensions as shown

in Figure 7. It was implicitly assumed that no secondary beams were placed orthogonally to the frame in order to ensure a three-dimensional response of the structure. Both columns and beams are made of C40/50 concrete with B450C steel rebar (yield strength f_y = 450 MPa [33]). The columns are reinforced longitudinally with 16 Ø20 steel bars and transversally with Ø8 two-arm stirrups at 10 cm spacing. The distributed load acting on the beam, including its weight and the load from the contributory area of the roof, is 26.9 kN/m, resulting in a total seismic mass of 73.42 ton evaluated according to the Italian Building Code (IBC) [33], and in a vertical force at either support of 360 kN, matching the design load of the DCS units.

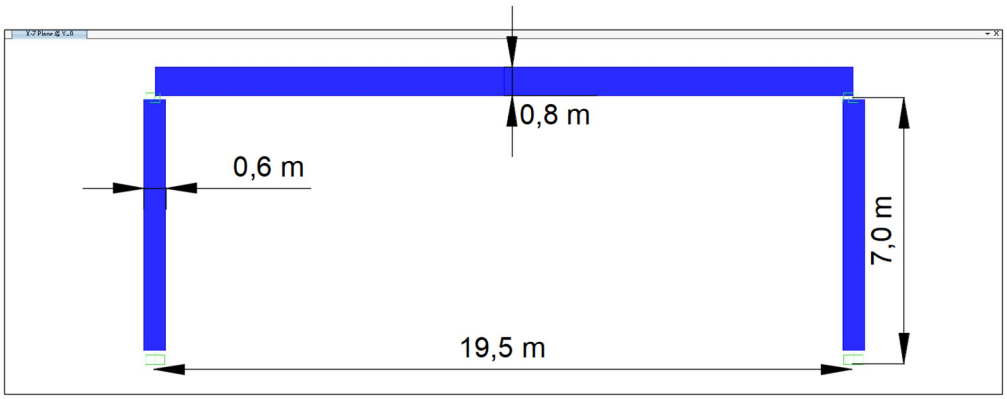

Figure 7. Portal frame model.

The structural model was implemented in SAP2000 v21.1.0 software [34]. The two columns were rigidly fixed to the ground and modelled as linear elastic elements, with a plastic (rotational) hinge at the basis formulated according to Table 10-8 (concrete columns) of ASCE 41-13 [35] in order to account for inelastic concrete deformation. The beam was assumed to behave as linear elastic, and a "*body*" constraint [34] was introduced to enforce equal displacement at both ends of the beam.

The connection between the beam and the column was modelled through a "*multilinear plastic*" link [34]. Two different models were formulated in order to represent the behavior of either the DCS or the beam-to-column pure friction connection:

- For the DCS, the force—deflection curve evaluated experimentally on the prototype was scaled up to the full size of the device; the hysteretic behavior was modelled by assigning a pivot hysteresis type, with hysteresis parameters: $\alpha_1 = \alpha_2 = 10^{10}$; $\beta_1 = \beta_2 = 0$; $\eta = 1$ (in the present framework, parameters α_1 and α_2 define the slope of the elastic branch of the load—deflection curve in either direction of loading, β_1 and β_2 define the force at zero displacement for unloading towards either positive or negative forces, respectively, and $0 \leq \eta \leq 1$ defines the amount of degradation of the elastic slopes after plastic deformation, where $\eta = 1$ means no degradation);
- For the beam-to-column pure friction connection, a constant friction coefficient μ_{cc} = 0.30, coupled to an isotropic hysteresis type, was assigned (it must be noted that, to be conservative, one half of the concrete-to-concrete friction coefficient recommended in Eurocode 8 [36] for smooth surfaces was adopted).

Though in the present analyses the backbone curve of the DCS represented in Figure 3c was modelled based on the experimental findings that will be presented in Section 4.1, different behaviors, such as the ones shown in Figure 3a,b can be simulated by combining multiple link elements as described in reference [37]; e.g., a multi-linear plastic link using the Pivot model is used to define the hysteresis loop, and a multi-linear elastic link [34] is used to shift the hysteresis loop away from the origin.

The fundamental period of the frame is T = 0.838 s. The internal structural damping is modeled as Rayleigh damping [38], with parameters assigned to achieve 5% damping ratio at frequencies f_1 = 1.1933 Hz (period T_1 = 0.838 s) and f_2 = 1.6366 Hz (period T_2 = 0.611 s).

Non-linear dynamic analyses were performed assuming a functional class c_U = II with nominal life V_N = 50 years, located in Potenza, south Italy (15.8094° longitude, 40.6435° latitude), topographic category T1, soil type B (deposits of very dense sand, gravel, or very stiff clay). The target elastic spectrum was determined according to the IBC Code [33] provisions for Life Safety Limit State (SLV), corresponding to hazard level with 10% exceedance probability in 50 years (reference period for ordinary buildings with V_N = 50 years and c_U = II). A set of seven unidirectional ground motions consistent with the target spectrum was selected with REXEL v3.4 beta [39] software from the European Strong-motion Database [40]. The magnitude (Mw) of the seven ground motions was chosen within the interval (6.4–7), with epicentral distance (Rep) in the range 0–30 km. The waveforms were scaled to the design Peak Ground Acceleration of 2.375 m/s^2 calculated according to the IBC [33]. Design spectral response acceleration is S_{DS} = 0.592 g in the constant acceleration region, and S_{D1} = 0.289 s at 1-s period. Relevant information on the ground motion data set is reported in Table 3, and the scaled horizontal spectra at 5% damping are shown in Figure 8. The average spectrum of the accelerogram set matches the target spectrum within a tolerance of −10/+30% in the period range 0.15–2.0 s, as recommended by the code [33].

Table 3. Accelerograms dataset.

Record	Waveform	EQ	Mw (-)	Rep (-)	PGA (m/s^2)	PGV (m/s)	SF
South Iceland	6263ya	1635	6.5	7	5.018	0.498	0.473
South Iceland (aftershock)	6328ya	2142	6.4	12	3.839	0.202	0.619
South Iceland	4673xa	1635	6.5	15	2.038	0.122	1.165
Montenegro	196ya	93	6.9	25	2.997	0.253	0.792
Campano Lucano	291ya	146	6.9	16	1.725	0.275	1.377
Montenegro	199	93	6.9	16	3.557	0.520	0.668
Campano Lucano	291xa	146	6.9	16	1.526	0.271	1.557
Mean			6.71	15.3	2.958	0.306	0.950

Mw: magnitude; Rep: epicentral distance; PGA: Peak Ground Acceleration; PGV: peak Ground Velocity; SF: Scale Factor.

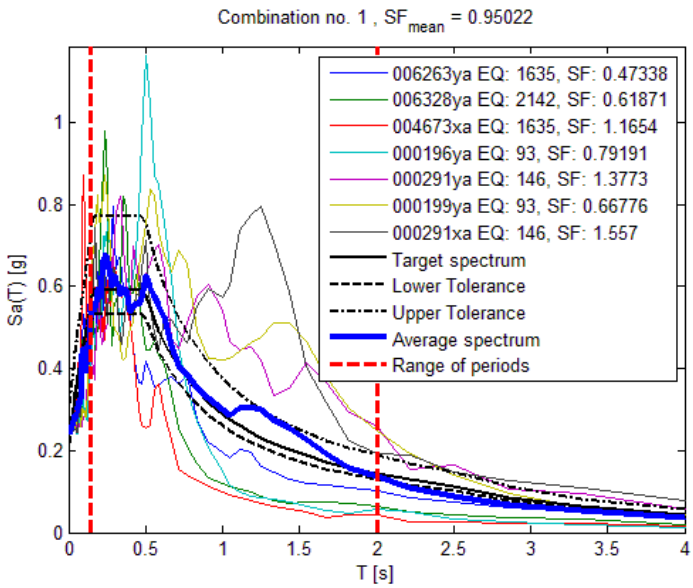

Figure 8. Scaled ground motion acceleration spectra and target spectrum according to the IBC (ξ = 5%) [33].

To be conservative, in the analyses an upward vertical component of ground acceleration of 0.4 g was further simulated, in order to reduce the horizontal reaction (for both the examined beam-to-column joints, i.e., the pure friction and the DCS, the resisting force

is proportional to the vertical load acting on the support) and trigger sliding at the beam-to-column interface. Consequently, the backbone curves of the multilinear plastic link elements associated to both connection types were recalculated accounting for a reduced vertical load of 216 kN (i.e., 60% of the full vertical load), and then coded in the structural model investigated in the analyses.

4. Results

4.1. Experimental Results

The shape of the force–deflection (F-d) diagram of the tested prototypes is shown in Figure 9 and actually resembles the theoretical curve for $\mu = \tan(\alpha)$ depicted in Figure 3c (the curve is also reproduced in Figure 9 as a dotted line). The plot is relevant to a single specimen and is obtained by dividing the experimental force measured in the test by two, assuming that the two specimens tested in pair provide the same reaction force.

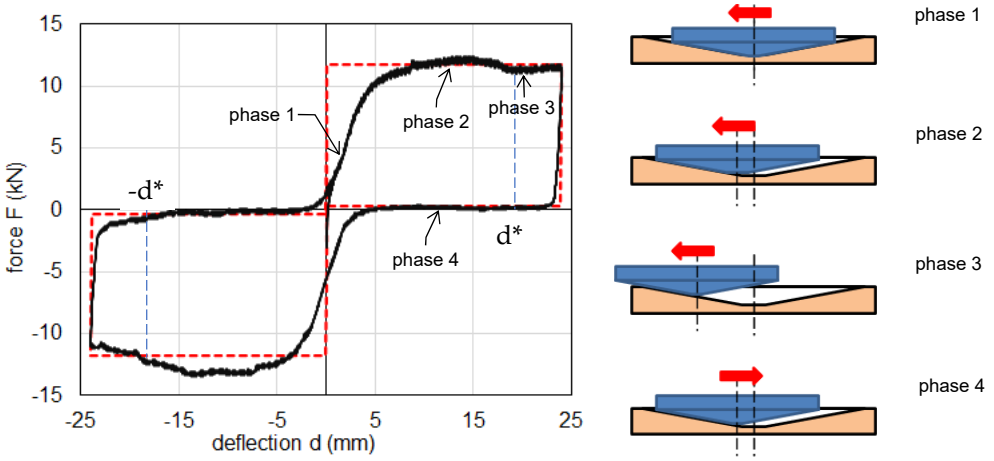

Figure 9. Experimental force—deflection diagram of the DCS, and different phases of motion.

The DCS exhibits a rigid-plastic behavior, characterized by four phases:

1. For small deflections, the force follows an almost proportional relationship with the displacement; this behavior is ascribed to the elastic deflection of the plates and the fixtures, before sliding is triggered between the mating surfaces of the convex and concave plates;
2. When the frictional resistance is exceeded, sliding is activated, and the response of the device is characterized by an almost constant force regardless of the deflection; in this phase the horizontal force of the system matches the theoretical value calculated according to Equation (1);
3. As the deflection exceeds a certain threshold d*, a shallow decrease of the horizontal force is noticed; when d = d* the convex plate reaches the boundary of the concave plate, and for larger deflections the actual contact area between the mating surfaces of the two plates decreases, increasing the contact pressure, which in turn affects the coefficient of friction;
4. During the return movement of the convex plate towards the origin the reaction force is virtually negligible; in this phase the restoring force due to the sloped surface and the friction force have opposite signs and balance each other, providing a null (or very small) resistance.

To identify the characteristic parameters of the system, two quantities are defined:

- Effective stiffness:

$$K_{eff} = \frac{F_{max}}{d_S}, \quad (2)$$

- Effective coefficient of friction:

$$\mu_{eff} = \frac{EDC}{4\, d_S\, N_S}, \quad (3)$$

where EDC is the energy dissipated per cycle (i.e., the area enclosed in the hysteresis cycle), F_{max} is the maximum force in the cycle, d_S is the maximum deflection, and N_S is the vertical load applied to the specimen. It must be noted that in general F_{max} is not achieved at the maximum deflection, and the definition of the effective stiffness given in Equation (2) conservatively overestimates the force at d_S; however, for the examined prototype the difference was very small (less than 5%) and therefore deemed as acceptable.

The effect of the vertical load on the mechanical behavior of the connection system was assessed in the static tests. The prototype was loaded up to 250% the (scaled) design value, without deterioration of its mechanical properties. The shape of the backbone curve is substantially unaffected by the vertical load (Figure 10a), and for $N_S \geq N_{d,s}$ the maximum force F_m increases almost linearly with N_S, in accordance with Equation (1), while at low load levels, the force tends to grow more than linearly. The effective stiffness and the energy dissipated per cycle show a fair proportionality with the vertical load up to 250% $N_{d,s}$ (Figure 10b), and the linear relationship is biased only at low loads. This behavior is explained in Figure 10c, where a certain influence of the vertical load on the coefficient of friction at low load levels is highlighted, while for $N_S \geq N_{d,s}$, μ_{eff} is very close to the design value of 0.10.

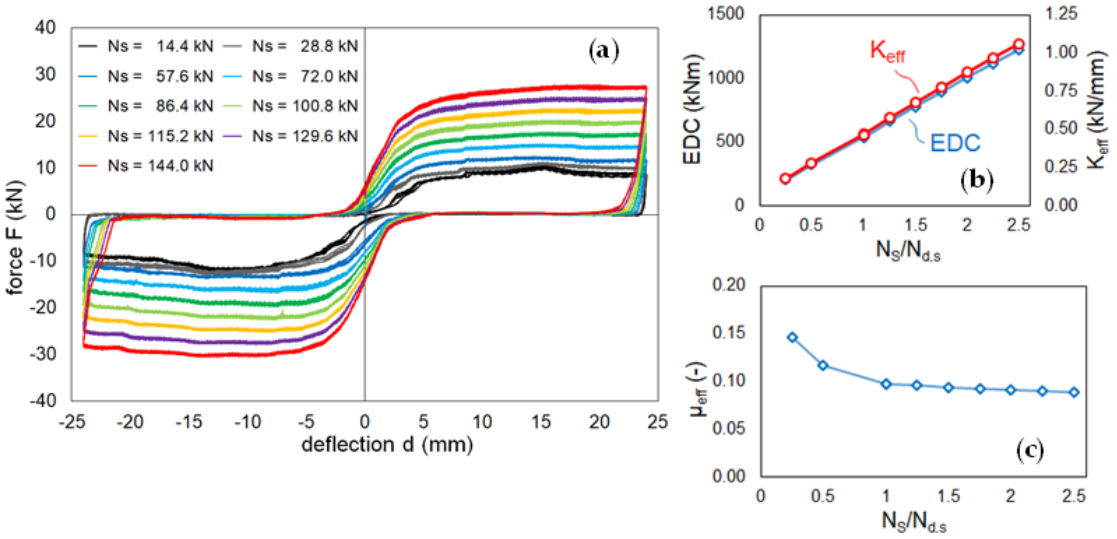

Figure 10. Static test (S): (**a**) horizontal force–deflection diagrams at different levels of vertical load N_S; (**b**) influence of the vertical load on effective Stiffness K_{eff}, energy dissipated per cycle EDC; (**c**) effective coefficient of friction μ_{eff}. $N_{d,s}$ is the design vertical load of the prototype.

The influence of the velocity was investigated in dynamic test D1. Increasing the speed from 3.36 to 33.6 mm/s on the scaled specimen (corresponding to a range of velocities from 5.3 to 55.3 mm/s on the full-scale system) does not significantly affect the overall shape of the force–deflection diagram (Figure 11a), resulting only in a 6% increase in the effective stiffness and in the energy dissipated per cycle (Figure 11b). The fluctuations observed in the test run at the highest speed highlight some possible stick-slip phenomenon at the sliding surfaces, but do not modify substantially the response of the system. Moreover, the effective coefficient of friction holds stable over the investigated speed range, with a maximum change of +7% from the lowest to the highest velocity (Figure 11a).

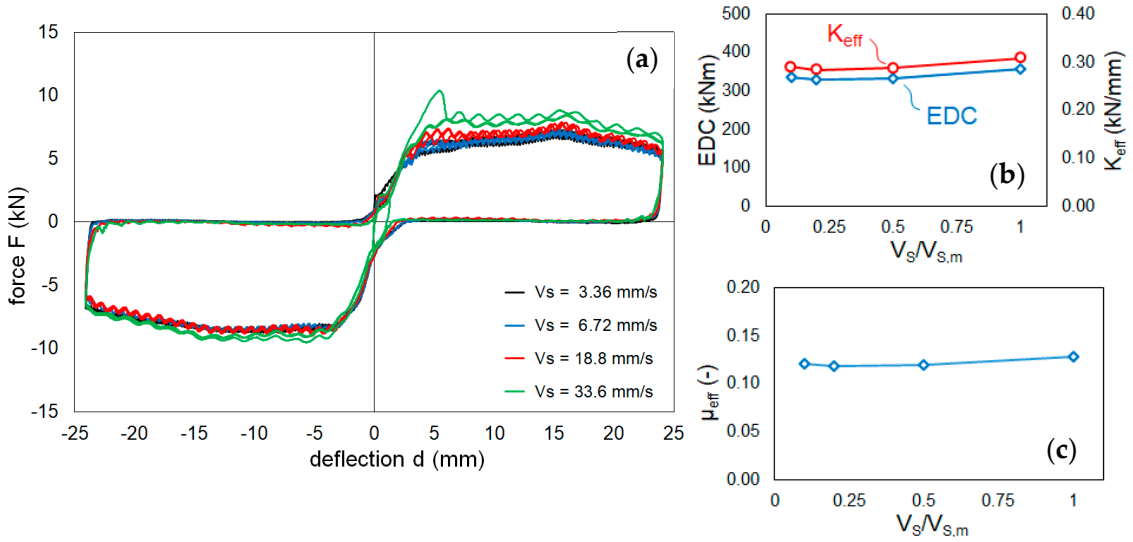

Figure 11. Dynamic test D1: (**a**) horizontal force–deflection diagrams at different velocities V_S; (**b**) influence of the velocity on effective stiffness K_{eff}, energy dissipated per cycle EDC; (**c**) effective coefficient of friction μ_{eff}. $V_{S,m}$ is the maximum test velocity.

In Dynamic test D2, the prototype was assessed to be able to perform 20 consecutive cycles to the design displacement $d_{bd,s}$ = 24 mm with a not substantial change of its performance (Figure 12a). The coefficient of friction increased by about 8% over the 20 cycles (Figure 12c), possibly due to the sweeping out of lubricant from the sliding surfaces (e.g., when the convex plate moves beyond the edge of the concave plate for d > d*). This resulted in a shallow increase (again on the order of 8%) in the effective stiffness and energy dissipated per cycle (Figure 10b).

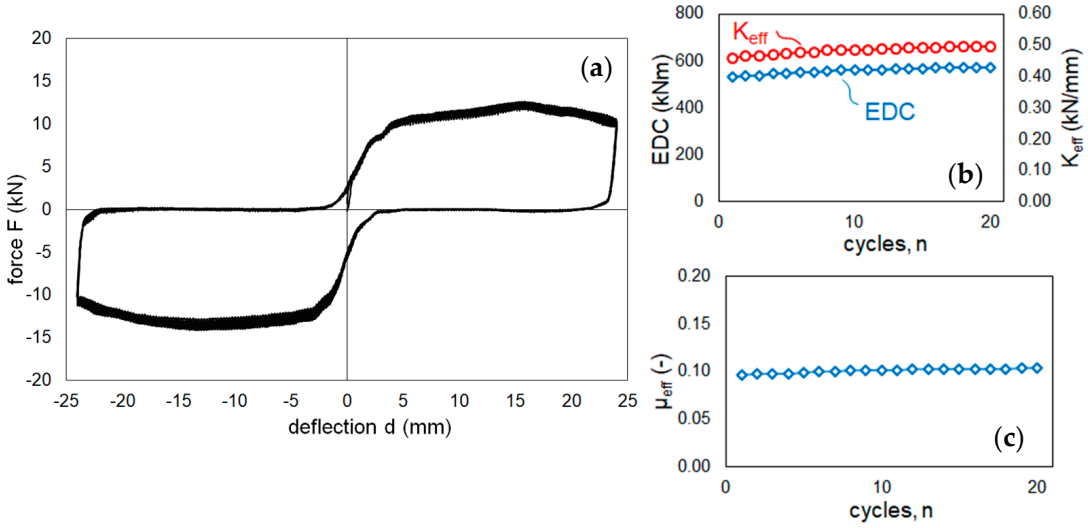

Figure 12. Dynamic test D3: (**a**) horizontal force–deflection diagrams; (**b**) change of Effective stiffness K_{eff} and energy dissipated per cycle EDC with the number of cycles; (**c**) change of effective coefficient of friction μ_{eff}.

The influence of the direction of sliding is shown in Figure 13. The shape of the force–deflection curve along a trajectory rotated by 45° (Figure 13a) is unvaried with respect to the shape of the curve observed for the on-axis trajectory (e.g., Figure 10a), with no substantial change both in energy dissipated per cycle (Figure 13b) and effective stiffness

(Figure 13c). Only at low load levels a light deviation is observed, possibly due to the influence of the contact pressure on the coefficient of friction.

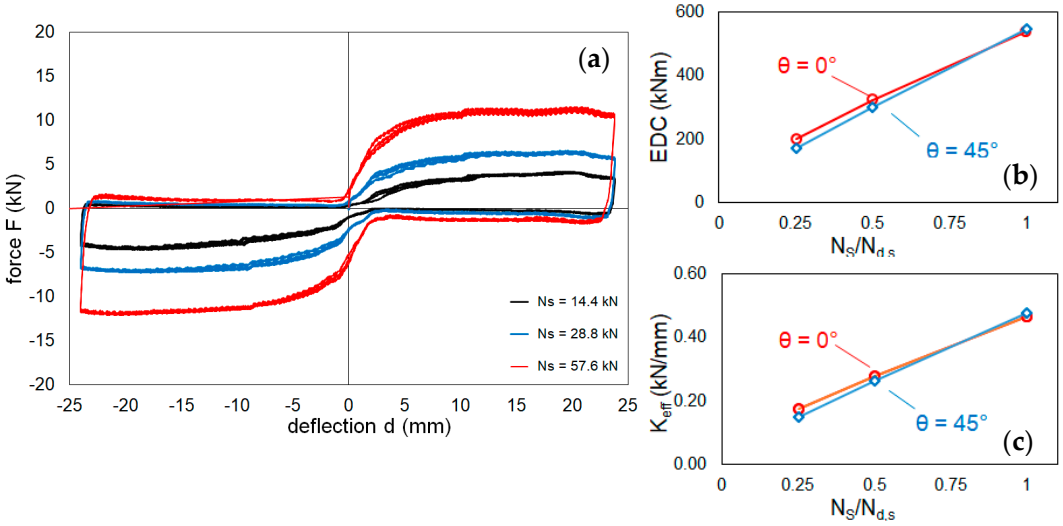

Figure 13. Static Test with Rotation (R): (**a**) horizontal force—deflection diagrams at different levels of vertical load; (**b**) energy dissipated per cycle edc and (**c**) effective stiffness K_{eff} along the rotated trajectory (θ = 45°) vs. on-axis trajectory (θ = 0°).

In conclusion, the experimental tests confirmed a stable and reliable behavior of the DCS, with a linear dependence of the maximum horizontal force on the vertical load in accordance with Equation (1), and a negligible influence of velocity and number of cycles.

4.2. Numerical Results

As an example of the output of the analyses, Figure 14 shows the relative displacement at the beam-to-column joint for either connection, DSC or pure friction (P-F), produced by a single accelerogram (record 196ya). Sliding of the P-F joint is engaged when the seismic action exceeds the friction resistance at the beam-to-column interface, and therefore occurs only during the strong motion stage of the earthquake. During the coda stage the ground acceleration is not sufficient to trigger sliding, and the beam remains in the offset position attained at the end of the previous stage. This leads to a huge residual displacement, d_{res}, close to the maximum displacement attained during the earthquake. In contrast, the DCS develops larger displacements during the strong motion stage (the peak displacement is 37 mm vs. 31 mm for the P-F joint), but owing to the restoring force provided by the sloped surfaces, it tends naturally to recover the original configuration as the ground acceleration gets down. For the examined earthquake, the residual displacement of the DCS is virtually null.

In general, similar results were obtained for all the examined accelerograms but for 4673xa record which was unable to engage sliding for both connections. In this case, while in the P-F joint the displacement of the beam was blocked, in the DCS small movements of the beam corresponding to elastic deformation of the connection system could take place, though energy dissipation was not activated in absence of sliding.

To compare the performance of the DCS to the one of the pure friction joint, the results of the non-linear dynamic analyses were evaluated examining both the behavior of the beam-to-column connection and the internal forces in the columns. During the post-processing of the results, the maxima of the response parameters were identified for each accelerogram, and the mean and standard deviation of the values were calculated for the set of seven ground motions.

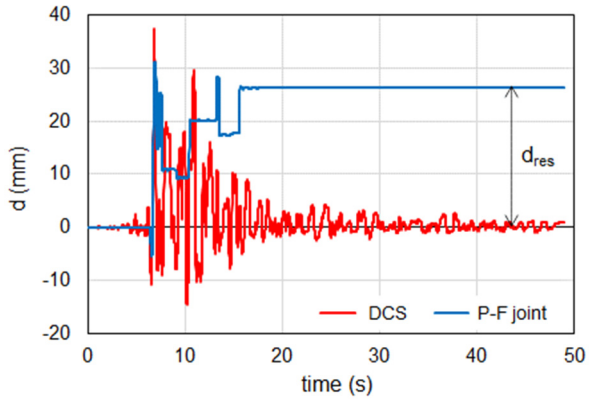

Figure 14. Displacement histories of the examined beam-to-column joints for record 196ya.

Figure 15 shows the maximum resisting force of the beam-to-column joint, F_{max}, the maximum horizontal displacement of the beam with respect to the column, d_{max}, and the offset, or residual displacement, of the beam, d_{res}, at the end of the ground motion, assessed for both connections.

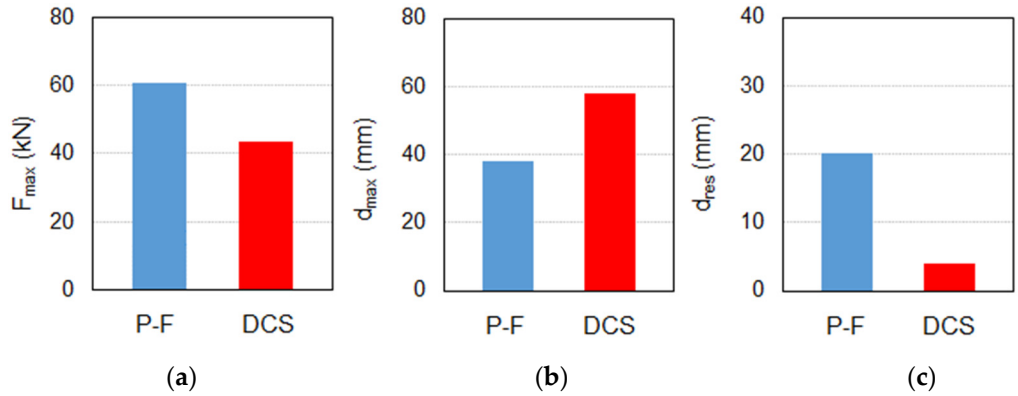

Figure 15. Comparison of the seismic response (averaged on seven ground motions) of DCS and pure friction (P-F) joint: (**a**) maximum force; (**b**) maximum displacement; (**c**) residual displacement.

By assuming a concrete-to-concrete friction coefficient $\mu_{cc} = 0.30$, the maximum force developed by the P-F joint is about 40% greater than the resisting force of the DCS with $\alpha = 6°$ and $\mu = 0.105$ (Figure 15a). Owing to the higher dissipation capability provided by the higher friction, the P-F joint better limits the displacement of the beam during the earthquake, with a maximum slippage of 38 mm vs. 58 mm (Figure 15b); nevertheless, it must be noted that the maximum displacement of the beam supported by the DCS, i.e., $d_{max} = 57.8$ mm, matches the design value $d_{bd} = 60$ mm of the system, and can therefore be accommodated by the mechanical joint. The fair recentering behavior of the DCS is highlighted in Figure 15c: at the end of the ground motion the offset of the beam is as small as $d_{res} = 4$ mm, i.e., 1/15 of d_{max}. In contrast, assuming a pure friction connection the offset of the beam is about 20 mm, i.e., 1/2 of the maximum displacement provided by the joint. Even though the connection can fit the seismic displacement of the beam without loss of support, residual displacements should be controlled, as they can accrue during sequences of ground motions occurring in short times, making reducing the capability of the structure to withstand aftershocks and future earthquakes.

Eventually, Figure 16 compares the maximum shear force, V_{max}, and the maximum bending moment, M_{max}, at the base of the column. As a consequence of the lower reaction force, the DCS induces smaller internal forces (about −11%) than the P-F joint, therefore limiting the stresses in the columns and at the foundation level. The base shear is reduced from 81 kN to 72 kN, and the moment from 572 kNm to 506 kNm.

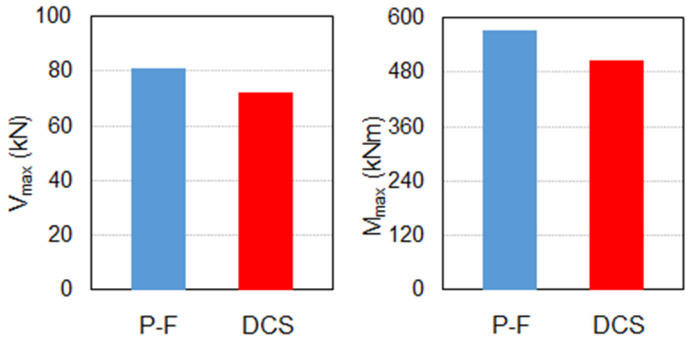

(**a**) (**b**)

Figure 16. Comparison of the seismic performance of DCS and pure friction (P-F) joint: (**a**) maximum base shear force in the columns; (**b**) maximum bending moment in the columns.

5. Conclusions

A dissipative connection system (DCS) for precast RC industrial sheds has been introduced both for new structures as well as for retrofit of existing facilities designed according to updated standards without seismic concepts. The system exploits the movement between two mating sloped surfaces to dissipate energy through friction and to generate a restoring force. In the study the force-displacement behavior of the DCS was investigated experimentally and non-linear dynamic analyses were performed to assess the effectiveness of the proposed system:

1. The force-displacement curve shows, after an initial elastic response, a constant force when the convex plate moves away from the center, and a negligible reaction when the convex plate returns towards the origin; the force, which is governed by the properties (slope angle and friction) of the sliding surfaces, increases linearly with the vertical load on the support but is scarcely affected by the velocity;
2. Non-linear dynamic analyses proved the effectiveness of the DCS to control the relative displacements at the beam-to-column joint, and the maximum shear force transmitted to the column head, thereby limiting internal forces and moments within the columns;
3. Owing to a certain restoring capacity provided by assuming $\mu = \tan(\alpha)$, the DCS was able to control the residual displacement at the end of the ground motion within small values (1/15 of the maximum displacement, in the examined case), thereby limiting the accrual of displacements during sequences of earthquake, which can hamper the capability of the structure to withstand aftershocks.

Though the numerical analyses have confirmed that viability of the DCS to control beam-to-column joint displacements, an improved version of the system with two distinct slopes of the concave and convex surfaces, namely $\alpha_1 = 6°$ in the central region of the plates and $\alpha_2 = 12°$ close to the edges, is under development. For small displacements, sliding occurs between mating regions of both surfaces with $\alpha_1 = 6°$, but when a certain displacement threshold is exceeded the contact shifts to mating regions with $\alpha_2 = 12°$, in order to increase the horizontal stiffness and prevent a further increase in displacement. This new version is intended to be used for strong seismic scenarios, in order to limit the increase in size of the plates that would be required to accommodate huge horizontal deflections.

Owing to the limits of the study, i.e., only one frame geometry and one design earthquake being investigated, the results need to be confirmed by a wide series of analyses considering different layouts and characteristics of the precast shed, as well as different seismic inputs, which will be the subject of a future work.

Author Contributions: Conceptualization, L.M.; Funding acquisition, L.M.; Investigation, V.Q.; Methodology, V.Q.; Software, C.P.; Supervision, V.Q.; Validation, E.B.; Writing—original draft, V.Q.; Writing—review & editing, C.P. and E.B. All authors have read and agreed to the published version of the manuscript.

Funding: This research was funded by the "Smart Living" grant of Regione Lombardia, project "E.N.E.A.—Efficienza nuova per l'energia e l'antisismico"—CUP: E28B17000020009".

Data Availability Statement: Data deriving from the current study can be provided to the readers based upon their explicit request.

Acknowledgments: The Authors thank Fabrizio Grillo for the sketches of the dissipative connection system.

Conflicts of Interest: The dissipative connection system is patented by L.M. The other authors declare that they have no known competing financial interests or personal relationships that could have appeared to influence the work reported in this paper. The funders had no role in the design of the study; in the collection, analyses, or interpretation of data; in the writing of the manuscript, or in the decision to publish the results.

References

1. Belleri, A.; Brunesi, E.; Nascimbene, R.; Pagani, M.; Riva, P. Seismic performance of precast industrial facilities following major earthquakes in the Italian territory. *J. Perform. Constr. Facil.* **2015**, *29*, 04014135. [CrossRef]
2. Belleri, A.; Torquati, M.; Riva, P.; Nascimbene, R. Vulnerability assessment and retrofit solutions of precast industrial structures. *Earthq. Struct.* **2015**, *8*, 801–820. [CrossRef]
3. Bosio, M.; Belleri, A.; Riva, P.; Marini, A. Displacement-based simplified seismic loss assessment of Italian precast buildings. *J. Earthq. Eng.* **2020**, *24*, 60–81. [CrossRef]
4. Artioli, E.; Battaglia, R.; Tralli, A. Effects of 2012 Emilia earthquake on industrial buildings of early '900 on the Po river line. *Eng. Struct.* **2013**, *56*, 1220–1233. [CrossRef]
5. Magliulo, G.; Fabbrocino, G.; Manfredi, G. Seismic assessment of existing precast industrial buildings using static and dynamic nonlinear analyses. *Eng. Struct.* **2008**, *30*, 2580–2588. [CrossRef]
6. Liberatore, L.; Sorrentino, L.; Liberatore, D.; Decanini, L.D. Failure of industrial structures induced by the Emilia (Italy) 2012 earthquakes. *Eng. Fail. Anal.* **2013**, *34*, 629–647. [CrossRef]
7. Belleri, A.; Moaveni, B.; Restrepo, J.I. Damage assessment through structural identification of a three-story large-scale precast concrete structure. *Earthq. Eng. Struct. Dyn.* **2014**, *43*, 61–76. [CrossRef]
8. Brunesi, E.; Nascimbene, R.; Bolognini, D.; Bellotti, D. Experimental investigation of the cyclic response of reinforced precast concrete framed structures. *PCI J.* **2015**, *2*, 57–79. [CrossRef]
9. Batalha, N.; Rodrigues, H.; Varum, H. Seismic performance of RC precast industrial buildings—Learning with the past earthquakes. *Innov. Infrastruct. Solut.* **2018**, *4*, 4. [CrossRef]
10. Casotto, C.; Silva, V.; Crowley, H.; Nascimbene, R.; Pinho, R. Seismic fragility of Italian RC precast industrial structures. *Eng. Struct.* **2015**, *94*, 122–136. [CrossRef]
11. Demartino, C.; Vanzi, I.; Monti, G.; Sulpizio, C. Precast industrial buildings in Southern Europe: Loss of support at frictional beam-to-column connections under seismic actions. *Bull. Earthq. Eng.* **2016**, *16*, 259–294. [CrossRef]
12. Italian Building Code. *Technical Recommendations for Design, Execution and Testing of Precast Buildings—D.M. 3/12/1987*; Italian Building Code: Rome, Italy, 1987. (In Italian)
13. Italian Building Code. *Technical Recommendations for Buildings—D.M. 14/01/2008*; Italian Building Code: Rome, Italy, 2008. (In Italian)
14. Mazza, F.; Mazza, M. Seismic retrofitting of gravity-loads designed r.c. framed buildings combining CFRP and hysteretic damped braces. *Bull. Earthq. Eng.* **2019**, *17*, 3423–3445. [CrossRef]
15. Bournas, D.A.; Negro, P.; Taucer, F.F. Performance of industrial buildings during the Emilia earthquakes in Northern Italy and recommendations for their strengthening. *Bull. Earthq. Eng.* **2014**, *12*, 2383–2404. [CrossRef]
16. Martinelli, P.; Mulas, M.G. An innovative passive control technique for industrial precast frames. *Eng. Struct.* **2010**, *32*, 1123–1132. [CrossRef]
17. Javidan, M.M.; Nasab, M.S.E.; Kim, J. Full-scale tests of two-story RC frames retrofitted with steel plate multi-slit dampers. *Steel Comp. Struct.* **2021**, *39*, 645–664. [CrossRef]
18. Javidan, M.M.; Kim, J. Steel hysteretic column dampers for seismic retrofit of soft-first-story structures. *Steel Compos. Struct.* **2020**, *37*, 259–272. [CrossRef]
19. Belleri, A.; Marini, A.; Riva, P.; Nascimbene, R. Dissipating and re-centring devices for portal-frame precast structures. *Eng. Struc.* **2017**, *150*, 736–745. [CrossRef]
20. Javidan, M.M.; Kim, J. Seismic retrofit of soft-first-story structures using rotational friction dampers. *J. Struct. Eng.* **2019**, *145*, 04019162. [CrossRef]

21. Sonda, D.; Pollini, A.; Cossu, M. Seismic retrofit of an industrial building using damping devices. *Struct. Eng. Int.* **2020**, *30*, 53–63. [CrossRef]
22. Dal Lago, B.; Naveed, M.; Tornaghi, M.L. Tension-only ideal dissipative bracing for the seismic retrofit of precast industrial buildings. *Bull. Earthq. Eng.* **2021**, *19*, 4503–4532. [CrossRef]
23. Morelli, F.; Piscini, A.; Salvatore, W. Seismic retrofit of an industrial structure through an innovative self-centering hysteretic damper: Modelling, analysis and optimization. In Proceedings of the ECCOMAS 2016 VII European Congress on Computational Methods in Applied Sciences and Engineering, Crete, Greece, 5–10 June 2016.
24. Quaglini, V.; Gandelli, E.; Dubini, P.; Limongelli, M.P. Total displacement of curved surface sliders under nonseismic and seismic actions: A parametric study. *Struct. Control Health Monit.* **2017**, *24*, e2031. [CrossRef]
25. Decanini, L.; Gavarini, C.; Mollaioli, F. Some remarks on the Umbria-Marche earthquakes of 1997. *Europ. Earthq. Eng.* **2000**, *3*, 18–48.
26. Huang, Y.; Wu, J.P.; Zhang, T.Z.; Zhang, D.N. Relocation of the M 8.0 Wenchuan earthquake and its aftershock sequence. *Sci. China Ser. D-Earth Sci.* **2008**, *51*, 1703–1711. [CrossRef]
27. Di Sarno, L.; Elnashai, A.S.; Manfredi, G. Assessment of RC columns subjected to horizontal and vertical ground motions recorded during the 2009 L'Aquila (Italy) earthquake. *Eng. Struct.* **2011**, *33*, 1514–1535. [CrossRef]
28. Di Sarno, L.; Yenidogan, C.; Erdik, M. Field evidence and numerical investigation of the Mw = 7.1 October 23 Van, Tabanli and the Mw > 5.7 November Earthquakes of 2011. *Bull. Earthq. Eng.* **2013**, *11*, 313–346. [CrossRef]
29. Motosaka, M.; Mitsuji, K. Building damage during the 2011 off the Pacific coast of Tohoku Earthquake. *Soils Found.* **2012**, *52*, 929–944. [CrossRef]
30. Carydis, P.; Castiglioni, C.; Lekkas, E.; Kostaki, I.; Lebesis, N.; Drei, A. The Emilia Romagna, May 2012 earthquake sequence. The influence of the vertical earthquake component and related geoscientific and engineering aspects. *Int. J. Earthq. Eng.* **2012**, *29*, 31–58.
31. Mari, L.; Quaglini, V.; Pettorruso, C.; Bruschi, E. Experimental and numerical assessment of isolation seismic device for retrofit of industrial shed. In Proceedings of the COMPDYN 2021 and 8th ECCOMAS Thematic Conference on Computational Methods in Structural Dynamics and Earthquake Engineering, Athens, Greece, 27–30 June 2021.
32. Harris, H.G.; Sabnis, G. *Structural Modeling and Experimental Techniques*, 2nd ed.; CRC Press LLC: Boca Raton, FL, USA, 1999.
33. Italian Building Code. *Technical Recommendations for Buildings—D.M. 17/02/2018*; Italian Building Code: Rome, Italy, 2018. (In Italian)
34. SAP2000. *Analysis Reference, Volume 1*; Computer and Structures Inc.: Berkeley, CA, USA, 1997.
35. ASCE/SEI 41-13. *Seismic Evaluation and Retrofit of Existing Buildings*; American Society of Civil Engineers: Reston, VA, USA, 2014.
36. EN 1998-1. *Eurocode 8: Design of Structures for Earthquake Resistance—Part 1: General Rules, Seismic Actions and Rules for Buildings*; CEN European Committee for Standardization: Brussels, Belgium, 2004.
37. Andrawes, B.; DesRoches, R. Unseating prevention for multiple frame bridges using superelastic devices. *Smart Mater. Struct.* **2005**, *14*, S60–S67. [CrossRef]
38. Chopra, A.K. *Dynamics of Structures*, 5th ed.; Pearson: London, UK, 2017.
39. Iervolino, I.; Galasso, C.; Cosenza, E. REXEL: Computer aided record selection for code-based seismic structural analysis. *Bull. Earthq. Eng.* **2010**, *8*, 339–362. [CrossRef]
40. Ambraseys, N.; Smit, P.; Sigbjornsson, R.; Suhadolc, P.; Margaris, B. Internet-Site for European Strong-Motion Data, European Commission, Research-Directorate General, Environment and Climate Programme. Available online: http://www.isesd.cv.ic.ac.uk/ESD/ (accessed on 24 November 2021).